Fused filament fabrication of Stainless Steel 316L: Investigation on effect of printing parameters on microstructural and mechanical strength of sintered part

Dr. SAGAR M BALIGIDAD[1,] Dr. BATLURI TILAK CHANDRA [2], GIRISH S M [3]

[1] Department of Mechanical Engineering, CMR Institute of Technology
[2] Department of Mechanical Engineering, Sri Siddartha of Technology
[3] Department of Mechanical Engineering, Sri Siddartha of Technology

Abstract- The fabrication of metal components by powder bed fusion and direct energy deposition is time- and energy-consuming and expensive. The filament extrusion AM-based technique uses a unique metal feedstock that combines a multi-component binder with sinterable metal powders, followed by de-binding and sintering to produce metal components at an affordable price. The polymeric binder is essential component for a successful fabrication part and to maintain its mechanical strength. This study describes the fabrication of stainless steel 316L (SS316L) components using the fused deposition modelling technique (FFFm) through a number of optimisation phases. The study also includes the investigation of possible influence of FFFm operating parameters (layer thickness (LT), layer shell (LS), and filament flow %) on the density, porosity, and mechanical properties of 3D printed SS316L parts. The structure, macrostructure, and mechanical characteristics of the FFFm 3D printed components (tensile test, flexural test, and microhardness) were investigated. A proper fusion between layers, complete fusion without oxidation, and the absence of flaws and undesirable geometries have all been validated by macrostructure at various zones. The results of tensile and flexural components produced with different operating parameters come within a range of values that are similar to the value of wrought SS316L. The part produced with 0.15 mm LT, a 4-LS, and a 120-filament flow% showed the highest UTS and elongation at break values of 464.1 MPa and 42% respectively and also, it exhibits maximum density. The specimen printed with 0.25 mm LT, a 2-LS, and 100 filament flow% had the lowest UTS and elongation at break values of 409.9 MPa and 37% respectively. Large dimples near to one another and layer delamination for the greater layer thickness were found in the SEM analysis of fractured tensile and fracture impact test specimen data. Thus, the as-built multi-layered structure's outstanding ductility was clearly demonstrated by the findings. Large dimples near to one another and layer delamination for the greater layer thickness were found in the SEM analysis of fractured tensile and fracture impact test specimen data. Thus, the as-built multi-layered structure's outstanding ductility was clearly demonstrated by the findings

Keywords: FFFm, 3D printing, mechanical properties, microhardness, SS316L.

I. INTRODUCTION

The Additive manufacturing (AM) technology is a versatile approach for producing intricate objects [1], and it is undoubtedly used for producing dense structures using the layer-by-layer manufacturing approach. Therefore, AM technology has gained interest in a different industrial field like automotive, aerospace, marine, and biomedical applications [2-4]. Powder/wire is used as a feedstock in AM technology to fabricate metal components, which are subsequently melted by a high-energy heat source. Several AM methods exist today for making metal components, but each has a unique set of restrictions [5]. Among all, the SLM approach is regarded as the most advantageous technique for metal printing, due to its processing benefits.

The laser source fully melts the selected powder particles in the SLM process, followed by particle re-solidification to make a final dense component [6]. However, the need of a laser or electron beam source makes this process expensive, and even the method used to generate free flowing powder adds to the material's cost. Furthermore, process-induced porosity, layer delamination due to residual stresses, and secondary brittle phase can all have a negative impact on the mechanical characteristics of AM-fabricated materials [7]. Hence, while the material extrusion process is commonly used to produce plastic components, few attempts are made to manufacture other types of materials such as metals and ceramics using this technology [8-11]. In the FFF process, metal feedstock will be produced by mixing metal powder with a polymeric binder to help shape, and the binder will be removed after deposition in a de-binding operation, leftover metal material is sintered further dense part [12]. However, few issues still unsolved, and the primary focus of FFF parts is on the microstructure and mechanical characteristics. In this regard, several investigations on the physical and mechanical characteristics of AM parts have been conducted. In the recent advancement, materials like aluminum, steel, and titanium,

have been utilized in the FFF 3D printing process [13]. The stainless steel 316L is most investigated and often used materials for FFF 3D printing due to its great corrosion resistance, weldability [14], and high thermal strength [15]. Several studies have been recorded on the mechanical anisotropy [16-20], surface roughness [21, 22], and fatigue [23] properties of SS316L.

Thompson et al. [24] studied the volume percentage of SS316L metal pieces, as well as its impact on the mechanical characteristics and microstructure of an FFF 3D printed part. By optimising process conditions, they were able to report that 55 vol% of metal displayed dense part. Ait-Mansour et al. [25] sought to 3D print commercial BASF SS316L components and investigated how printing variables such as infill density (25% to 125%) and build orientation (flat, upright, and sideways) influenced mechanical and shrinkage behaviour. The porosity of the final microstructure of the sintered item was measured. Tosto et al. [26] investigated the mechanical properties of Ultrafuse 316L tensile specimens which are 3D printed in two directions (flat and upright). The flatwise build part demonstrated highest mechanical properties than other. Carminati et al. [27] investigated yield strength, elongation at break of Ultrafuse 316L components, and also to quantify the influence of the sintering phase on the microstructure. The part printed at 0.1 mm LT and speed of 20 mm/s depicts highest density of 95%. Marius A. Wagner et al. [28] developed SS316L for FFF 3D printing utilising different polymer binder components such as LDPE and TPE. The authors noticed that increasing binder concentration makes the feedstock more complicated and harder to achieve desirable qualities in the final metal component, which raises the challenge in the binder selection process. Anirudh Kasha et al. [29] investigated the use of ultrafuse 316L material in 3D printing flexural strength test samples with varying print parameters (raster angle and layer thickness) and flat print location. The team is successful in developing specimens with the fewest voids and porosity following the sintering process. Alessandro Pellegrini et al. [30] used digital image correlation (DIC) to investigate the mechanical behaviour of 3D printed SS316L parts. The final microstructures, and hence the resulting properties, are significantly determined at the sintering step. Although material tribological performance is a significant factor in engineering design, limited research has been conducted to investigate the tribological functioning and wear mechanics of AM printed SS316L parts. Sun et al. [31] investigated the tribological properties of SLM-printed SS316L samples at various laser scan speeds. The investigators were able to print the part with porosities varying from 1.7 to 6.7% with decreased dry slide wear resistance. Sander et al. [32] studied and compared the wear, mechanical, and microstructural aspects of SLM printed FeCrMoVC tool steel parts to casting parts. SLM components had stronger hardness and compressive strength while having a reduced wear rate and fracture strain, according to the results. Bartolomeu et al. [33] compared the mechanical and tribological parameters of SLM printed SS316 parts to those of hot pressing and standard casting processes. The results demonstrated that SLM parts had higher yield strength, wear resistance, and hardness than the other two methods.

Given the preceding, it is safe to assume that no reports have been made and no study on the tribological behaviour of 3D printed SS316L components made using the FFF technique has been done. The study fallows a systematic method to examine the impact of process variables and sintering conditions on the tribological performance of SS316L components. Furthermore, the parts microstructure, hardness, toughness, and even phase shift in the final materials are examined.

II.   Materials and methods:

In this experiment, stainless steel (SS316L) filament diameter of 1.75mm of make Colid from chain was used. The filament has a greater percentage (83.7%) of SS316L metal with a density of 3.4 g/cm3 and the remainder of PLA as a backbone binder and LDPE of grade PE35 as a soluble binder. Test samples were 3D printed by using the FFF process on a Creatbot F430 printer. Printing trials on SS316L parts were done with 0.4 mm diameter carbide nozzle. During the process, the nozzle and bed temperatures of 250 0C and 80 0C respectively, were maintained (Fig 1).
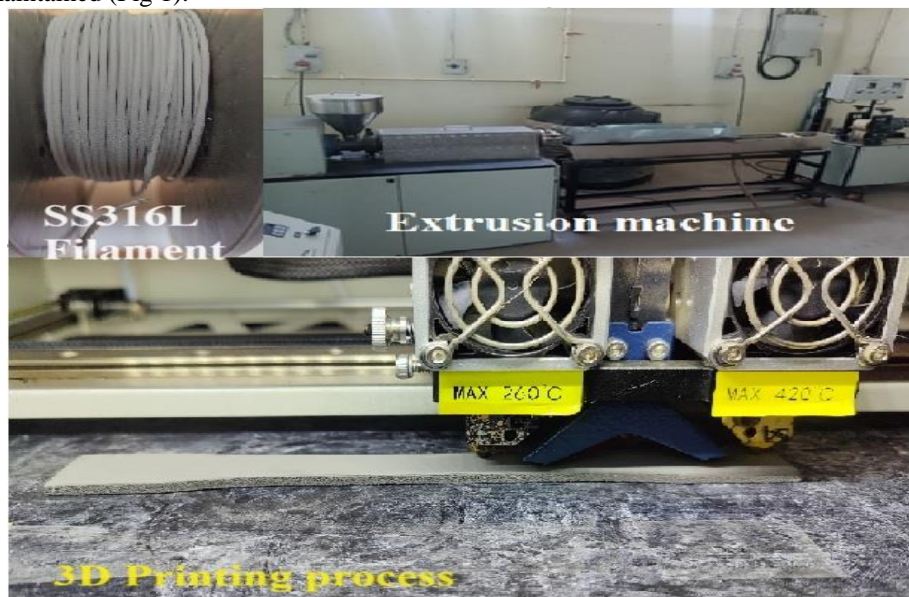
Fig 1. Experimental set up

It works by feeding a continuous filament through a direct drive extruder, pushing molten material through a heated nozzle, and then depositing layer by layer on the bed as specified by the CAD design. Following preliminary testing, Table 1 shows the primary printing parameters that were used to produce all of the samples.

Table 1: Primary 3D Printing parameters

Parameters	Value
Carbide Nozzle size	0.4 mm
Filament diameter	1.75 mm
Nozzle temperature	250 0C
Bed Temperature	80 0C
Print Speed	30 mm/sec
Extrusion width	0.4 mm
Fill density	100%

The arrangement of the dimensions and geometry of the "green" specimens (length: x, width: y, and thickness: z) are displayed in Fig 2.
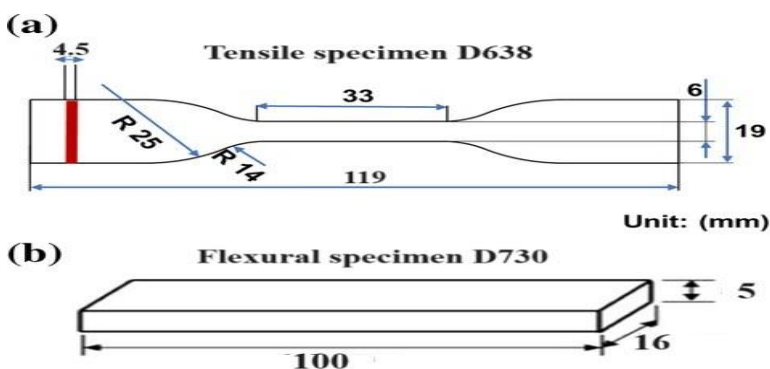

Fig 2. Dimensions of tensile and flexural test specimens

The flatwise orientation (xy build plate plane) was employed for printing the tensile (dog-bone) and flexural specimens. In this examination, different FFFm parts were printed at different operating parameters and all set of parameters are showed in Table 2.

Table 2: FFFm operating parameters of

	Layer Height (mm)	Layer shell	Filament Flow %
Samples 1	0.15	2	100
Samples 2	0.2	3	110
Samples 3	0.25	4	120
Samples 4	0.15	3	110
Samples 5	0.2	4	120
Samples 6	0.25	2	100
Samples 7	0.15	4	120
Samples 8	0.2	2	100
Samples 9	0.25	3	110

A consolidated green component is created using the above-described manufacturing process. To make a solid part, the green part is sintered at a temperature lower than its melting point, allowing the polymer binder to be removed and metal particles to sinter. The sintering procedure was performed in two phases with two holding cycles to get a dense component with required physical and mechanical qualities. Parts were also treated to a solvent de-binding procedure, which involved immersing them completely in cyclohexane organic solvent at 65 0C for 24 hours. To improve the transit rate of the degraded polymer chains, a magnetic stirrer revolving at 120 rpm was used. In this process, the soluble polymer/cyclohexane ratio was kept low to minimise saturation effects in the solvent. Further, the parts were air dried for 24 hours. The weight of the parts was measured before and after de-binding process in order to test the progress of polymer removal. Parts that remain after the de-binding procedure are referred to as "brown parts". Following the de-binding step, brown parts were sintered at 1310 0C in a vacuum (H2) furnace at a heating rate of 5 0C/min, which was maintained for 8 h before being allowed to cool within the furnace.

The goal of this study was to look at the effect of operating factors including fill density, build direction, and filament flow rate on component strength. ASTM D638 type IV and D790 standards were used to produce tensile and flexural test specimens.

Using a digital vernier calliper, the dimensions of each sample were measured in the X, Y, and Z axes. Both green and sintered samples underwent the measurements. This made it feasible to compute the samples' dimensions and volume both before and after the heat treatments. To ensure procedural accuracy and prevent unforeseen errors in measurements, the measurements were performed three times. Following that, the analysis's reference values were the average values. Using Equation (1), the shrinkage resulting from the de-binding and sintering processes was computed as the percentage dimension decrease in each of the three directions.

$$\text{Shrinkage (\%)} = \frac{(D_{Green} - D_{Sintered}) \, X \, 100}{D_{Green}} \qquad (1)$$

Where, DGreen and DSintered refers to the dimensions of green and sintered parts respectively. To assess the shrinkage rate caused by material loss during the sintering process, parts with particular dimensions were manufactured. Based on the change in dimensions along three dimensions, a scale multiplier will be applied to the actual dimensions, and components will be fabricated correspondingly for mechanical property evaluations. The final parts were examined to determine the best de-binding and sintering conditions. Prior to the mechanical tests, the density [20] (ρ) of green and sintered parts was determined using Archimedes' principles. The densities were determined using the samples' weight (g) and volume (cm3). With the use of a precision weighing machine and calliper, the weight and dimensions of sintered and green components were measured, and the average values were taken into account in the calculation:

$$\text{Density } (\rho)\text{green (g/cm3)} = \frac{Weight_{green}}{Volume_{green}} \qquad (2)$$

$$\text{Density } (\rho)\text{sintered (g/cm3)} = \frac{Weight_{sintered}}{Volume_{sintered}} \qquad (3)$$

A Rockwell hardness tester was used to perform hardness testing in accordance with the ASTM E18 standard. The mean value was calculated by taking five measurements for each sample. Prior to each test, the surface roughness was assessed using a contact profilometer at three distinct places.

Using optical and electron microscopy, microstructural analysis was done. Light microscopy was used to study the sintered microstructure of the components (Zeiss, Germany's AX10 Imager.M2m). The parts were polished using 320, 800, 1200, 2400, and 5000 grit SiC paper, followed by 3 µm diamond and 50 nm alumina suspensions. SEM (TESCAN-VEGA3 LMU) and energy dispersive X-ray analysis (EDX) (Ametek-EDAX detector) were also used to examine sintered microstructures. It is noted that the EDX maps shown here were post-processed to increase the visibility of the regional variation in chemical composition.

Large scale tensile and flexural tests, were performed on specimens sintered according to Table 1. Universal testing machine (Schenck RSA 100, Schenck, Germany) equipped with a 100 kN load cell at a strain rate of 0.1 min−1. The strain for all the samples were measured optically.

III. Results and Discussion

Shrinkage behaviour

The flexural and tensile dimensions of every sample were measured after sintering. Table 3 displays the average shrinkage values along each axis.

Table 3: Average shrinkage% value of all specimens

	Tensile test specimen			Flexural test specimen		
	X-axis	Y-axis	Z-axis	X-axis	Y-axis	Z-axis
Samples 1	13.96	9.625	5	16.09	10.74	4.22
Samples 2	14.57	10.875	4.2	17.29	12.11	6.00
Samples 3	14.06	10.125	4.2	15.61	12.53	5.33
Samples 4	13.26	9.1875	6.6	15.94	12.26	3.33
Samples 5	14.09	7.625	6.4	16.12	10.63	2.89
Samples 6	13.86	11.625	5.8	16.78	13.95	1.78
Samples 7	12.86	6.375	7.4	16.24	11.68	2.67
Samples 8	13.92	8.9375	4.2	16.85	10.63	3.33
Samples 9	13.44	6.3125	4.2	15.96	13.89	6.89

Anisotropic shrinkage behaviour was shown by all specimens, suggesting that the FFFm operating parameters affect the shrinkage behaviour. The flexural specimens' average percentage shrinkage varied from 12.86 to 14.57% along the x axis, 7.56 to 11.63% along the y axis, and 4.2 to 7.4% along the z axis. The lowest percentage of shrinkage occurred in the tensile (dog-bone) specimens along the z axis, ranging from 1.78 to 6.89%, and different shrinkage percentage ranged from 15.61 to 17.29% along the x axes, 10.63 to 13.95% along the y axes. It makes sense that the specimens that shrivelled the most in their various sintering directions were those that were sintered along their thickness (z axis) for the flat build direction and along their breadth (y axis) for the tensile and flexural specimens

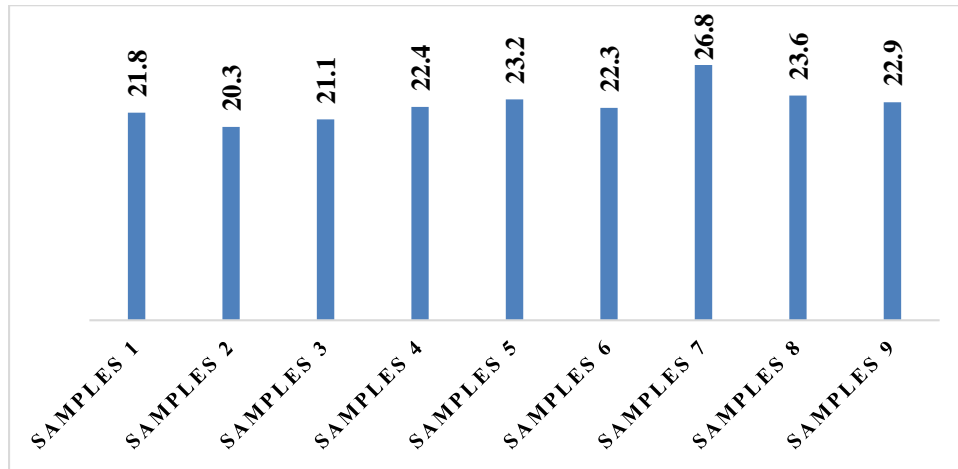**Hardness, Roughness and Density analysis**

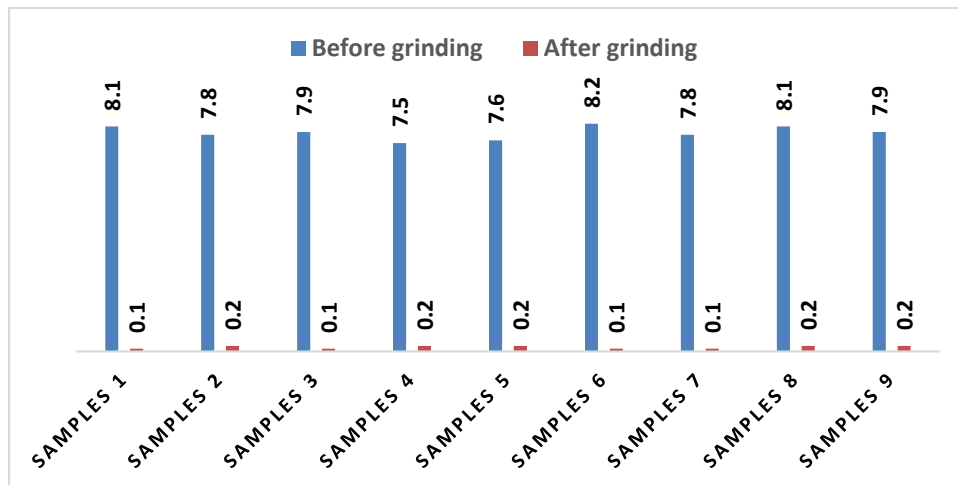Fig 3. Hardness all SS316L sintered parts

Fig 4. Surface roughness of all SS316L samples before and after grinding process

Fig 3 and Fig 4, demonstrates the hardness and surface roughness of all SS316L samples fabricated under different operating parameters. The results indicated no significant variance in Rockwell C hardness across all sections. Since FFFm components had a rough surface finish that deviated from typical manufacturing techniques, all specimens were ground and polished to smooth the surfaces. The hardness was measured in five different locations, and it was found that altering the operating parameters had no effect on the hardness, which had a uniform distribution. Porosity is a common issue in FFFm parts that negatively affects their mechanical properties. Fig 5a shows the porosity of samples taken by microscopic and SEM images. Delamination due to un-sintered metal particles visible between perimeter and infill. In addition, lack-of-fusion between the layers due to incomplete de-binding of binder that leads to the delamination of layers Fig 5b.
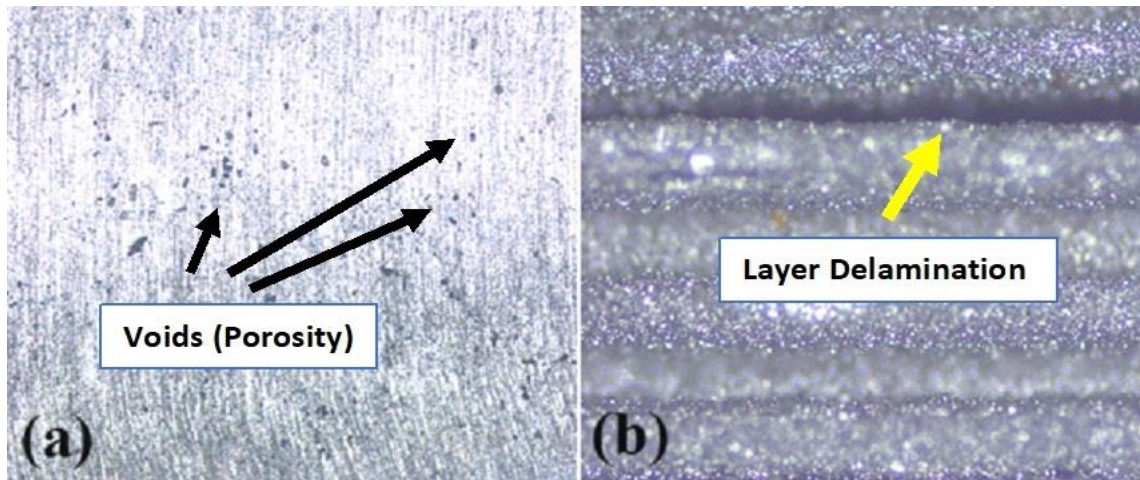
Fig 5: Porosity evaluation

The porosity condition of each sample influences hardness and density to some amount. For example, in a Rockwell hardness test, when the diamond tip touches the surface with pores underneath the surface, the volume of the holes can be compressed, resulting in a lower hardness value. The density of green and sintered parts was computed from Eqs. (2) and (3). Densities were found to be identical for corresponding green and sintered parts, with just a few minor variances, and a strong correlation between green and sintered parts was discovered, as indicated by red circles. Furthermore, the density of sintered parts was grouped based on their layer thickness (Fig. 6).
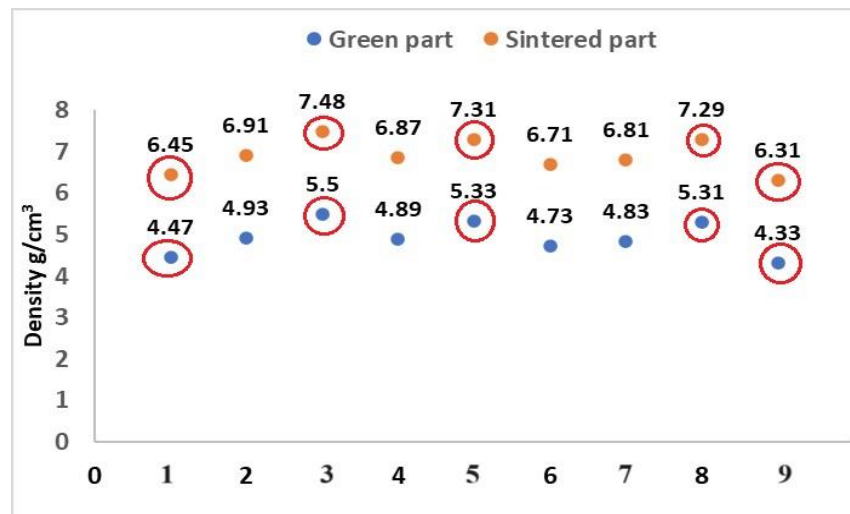

Fig 6: Density of sintered specimens

The 0.15 mm layer thickness with 120% filament flow resulted in the highest density values, with a minimum of 6.45 to highest of 7.48 g/cm3. In the same set of specimens, the values for the other two configurations, such as 0.2 mm and 0.25 mm layer thickness, were somewhat lower yet varied. The 0.2 mm layer thickness with 120% filament flow wall layers had a high variability (6.70-7.31 g/cm3), but the other two designs had smaller and less variable values. The 0.25mm layer thickness with 120% filament flow showed almost similar densities to 0.15mm and 0.2mm (7.29 g/cm3), but the 100% filament flow specimens showed a least density among all. In general, the layer thickness and number of wall layers impacted the sintered density for all configurations. Cross sections of the tensile specimens highlighted and are presented in Fig. 7 were viewed using an optical microscope (magnification of 140x) for a more comprehensive investigation and to get insight into the void's distribution in the manufactured portions.
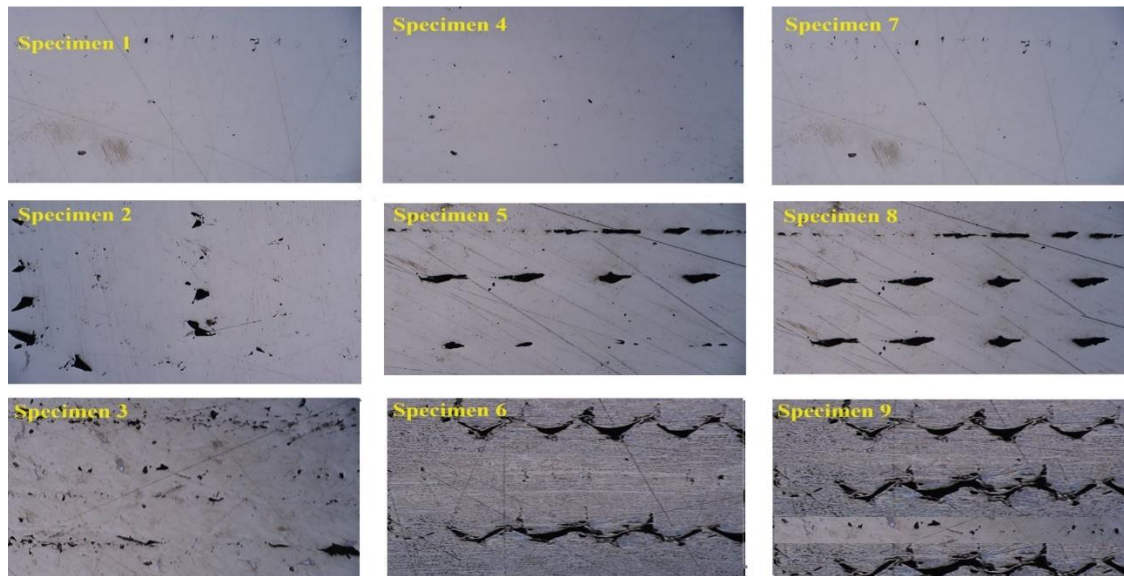
Fig 7: Sectional view of tensile test samples

Cross sections parallel to the layer thickness (Fig. 7) were specifically studied. The FFFm printing pattern creates voids at infill and internal perimeter meeting sites, resulting in porosity after sintering. As a result, it is critical to analyze the cross section of sintered parts in order to evaluate porosity, which is done after the pictures have been binarized. The voids mostly concentrated at between successive layers adhesion, between perimeter and infill pattern adhesion. As a result, porosity was determined as a percentage of the ratio of dark area to total area and is shown in Table 1. In comparison to 100% and 110% fill density, the part printed with 0.15 mm LT and 120% flow % (specimen 1) had the least porosity. The porosity of the 0.2 mm LT component printed with 120% fill density was 2.72%, whereas the porosity of the 0.2 mm LT part produced with 100% fill density was 4.05%. When the item was printed with 0.2 mm LT and varying fill densities, the porosity ranged from 2.72% to 4.61%. Similarly, the porosity range for the component printed with 0.25 mm LT with varying fill densities was 3.28% to 5.30%. The part printed with 0.25 mm LT had more porosity than the parts printed with 0.15 mm and 0.2 mm LT, and the porosity decreased when the fill density was raised from 100% to 120%. The porosity values for 0.15 mm LT parts, on the other hand, were much lower. These results agree with the porosity estimates obtained using Archimedes' fundamental measurements. The way of printing of material, deposition of layer on top of another layer result in part printed with greater LT have increased porosity. Furthermore, adhesion between consecutive layers might be hampered by temperature and surface property variations between each layer. This can result in weaker layer bonds and the creation of porous patches.

Mechanical properties Analysis:

Fig 8: Sintered tensile test specimens printed at different operating parameters

Fig 8 shows examples of all the sintered SS316L tensile test parts manufactured under the specified operating conditions. Tensile properties such as yield strength, ultimate tensile strength (UTS), and elongation at failure of all parts are presented in Table 4 and compared with reported values of monolithic AISI 316L to evaluate the relative mechanical performance of the FFFm SS316L parts in

an as-built condition with different operating parameters. The SS316L material employed in this work, according to both mechanical statistics, is similar to the values for bulk SS316L, even exceeding the elongation at failure.
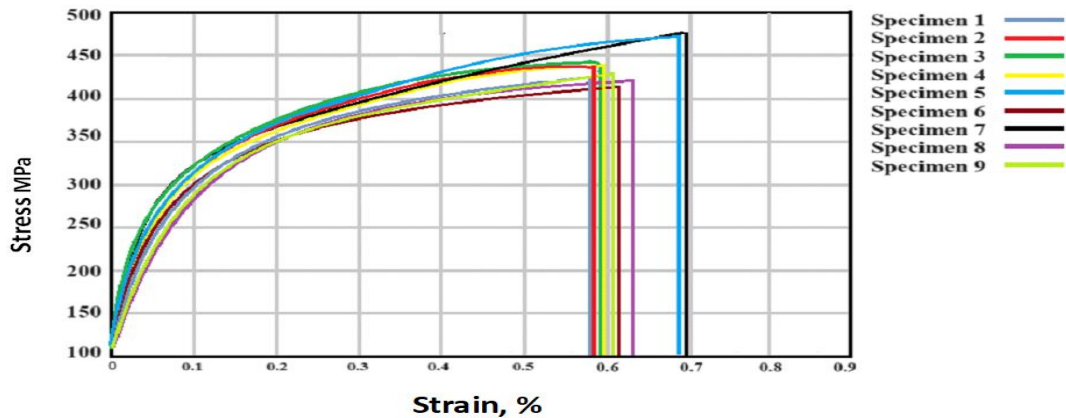

Fig. 9: Stress-strain curve of all sintered tensile test specimens

Fig 9 demonstrated the stress-strain curves of all the fractured parts. A careful review of the fractured parts reveals that the failure happened at identical areas and differences in behaviour was noticed in the elastic and plastic properties of the parts 3D printed at different operating parameters; these could be corelated with and attributed to the infill flow and layer thickness.

Specifically, the average yield strength (141.1 MPa) was reduced by 17% and the average UTS (426.6 MPa) was reduced by 12% compared to monolithic material due to the larger evenly spaced grains and full austenitic material structure after the sintering phase [34, 35].
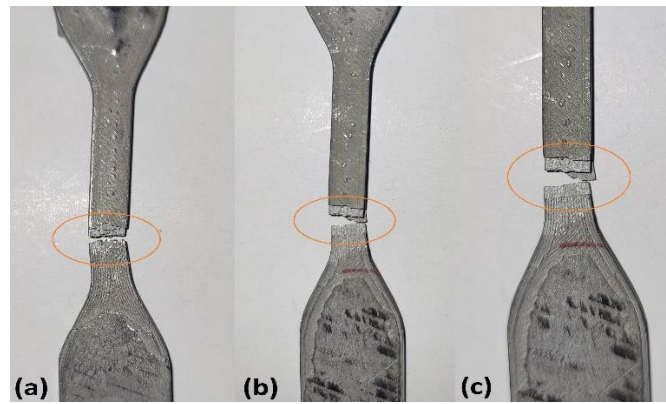

Fig 10: Cross-sectional view of the fractured neck section of

Fig 10 the elongation at break of AM components made of very near monolithic material, particularly open monolithic material, may reduce the ductility of AM specimens due to local stress concentrations. In the elastic region of the stress-strain curve, a part printed at 0.15 mm LT with 120% flow (specimen 7) had the highest UTS of 464.1 MPa, while the parts printed at 0.2 mm with 100% flow and 0.25mm LT with 100% flow had lower values of 412.1 MPa and 409.9 MPa, respectively, with corresponding elongation of 42, 30, and 37%. Fig 10 depicts a cross-sectional view of the fractured surface's neck portion of the samples. Different neck fracture mechanisms were identified and emerge along the middle axis near the neck. To validate the obtained results, the test results were compared to the results from literatures, which are shown in Table 4.

Table 4: Tensile and Flexural properties of SS316L parts

	σf (MPa)	UTS (MPa)	Elongation at Break (%)	Flexural strength (σf) MPa
Samples 1	117.3	418.1	32	611.6
Samples 2	122.9	429.3	31	629.8
Samples 3	125.0	447.3	38	636.2
Samples 4	130.3	435.8	37	679.9
Samples 5	134.6	455.2	39	701.9
Samples 6	131.7	409.9	37	753.4
Samples 7	132.9	464.1	42	815.4
Samples 8	155.7	412.1	30	787.9
Samples 9	160.2	420.8	33	774.6
AISI316L [39]	170	485	60	875.5

The yield and tensile strength reached were a bit lower on an overall basis than the other values given; however, the ductility achieved the highest level as compared to the values accessible in the literature. Tensile curves, as shown in Fig 9, exhibit a comparable pattern, illustrating the repeatability of the printing process. The difference in UTS and elongation at break between samples, on the other hand, indicates the existence of defects (voids and residual stress as a result of thermal processes). During the experiments, no substantial necking phenomena was found.

The mechanical parameters obtained here are notably different from those reported for more common SLM-based technique, which generally display lower ductility and greater ultimate strength. The discrepancy can be addressed by the unstable microstructures brought about by SLM-based technique, which display tiny microstructures of solidification cells and columnar grains, which are known to have strengthening effects while decreasing ductility. FFFm sintered parts showed a more homogenous grain structure and a near-equilibrium microstructure. Hence, they have lesser strength and can withstand larger failure stresses and also parts demonstrated dimpled morphology showing extensive micro-void coalescence.

Fig 11: Dimples formation during sintering process

In addition, particulate oxides are frequently observed inside dimples, (Fig 11) where they serve as nucleation sites for micro-voids. In view of the application of optimum operating parameters during the printing and sintering processes, the aforementioned analysis indicated superior and enhanced characteristics of FFFm SS316L parts. Massive pores noticed between neighbouring layers, on the other hand, are a primary cause of anisotropy in SS316L parts manufactured by FFFm. The material characteristics are isotropic if this process-induced porosity can be avoided by optimising the deposition settings.

Flexural Strength

Fig 12: Sintered flexural test specimens printed at different operating parameters

Fig 12 shows examples of all the sintered SS316L flexural test parts manufactured under the specified operating conditions. All of the specimens studied exhibited irregular plastic behaviour until a point beyond the plastic zone where a sharp spike in the force/deflection plot occurs, followed by a gradual drop in the plot.
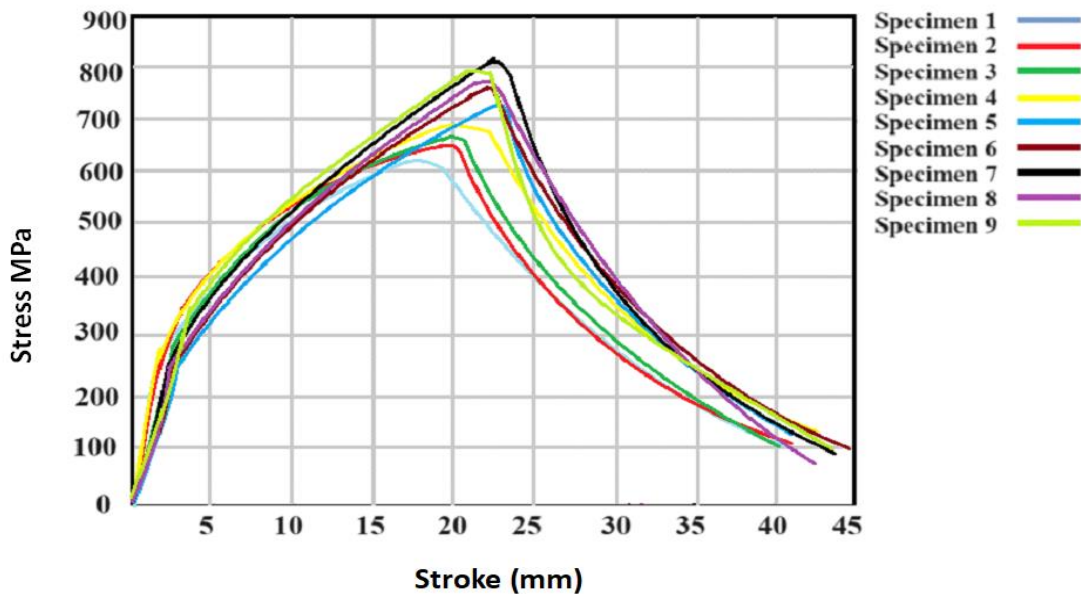

Fig. 13: Stress-stroke curve of all sintered flexural test specimens

The stress-stroke curves obtained from the bending test are depicted in Fig 13, and it was discovered that tensile stress was induced on the outer curve (convex side) of the specimens above the neutral axis, while compressive stress was induced on the inner curve (concave side) of the specimens below the neutral axis.

Fig 14: Parts after bending test

Fig 14 depicts one of the produced specimens following the flexural bending test. The ductility of the specimens is also seen in the load-deflection curve. The flexural strength properties of SS316L 3D printed parts with different combination of parameters are provided in Table 4. The results reveal that the investigated FFFm fabrication parameters—the 'layer height' and the 'flow percentage'—have an effect on flexural strength values. For example, the maximum flexural strength (σf) of the specimens printed '120% flow and 0.15mm LT' (sample 7) is 815.4 MPa, and flexural strain was around 44% on average, with a standard deviation of 1.4, as compared to 611.6 MPa for those printed '120% flow and 0.25mm LT (sample 1). Variations in σf values in SS316L specimens, including between LT, flow%, and perimeter shell
(Table 4), confirm the impact of the varied manufacturing process (specimen undergoing through de-binding and sintering process) on flexural strength values.

Flexural strength can be gauged by the type of tests applied and the structural properties of the samples 3D printed using the FFFm process. The majority of the strain in the bending test was concentrated in a small area above the neutral axis. The metal 3D printing method and subsequent thermal treatments introduce an intrinsic percentage of porosity into the specimens, which is especially sensitive to defect content. Due to the limited gauge area as compared to tensile specimen, the statistical chance of identifying open and closed porosities in the samples is low. The reproducibility of the method was shown by a similar pattern for all of the curves, and all of the greatest stress readings were made at about 12 mm of specimen deflection under bending pressure. All of the samples showed full deformation without the occurrence of fractures in the tensile stress region. Overall, the findings in Table 4 show that the mechanical strength is not comparable, even when the specimens are manufactured under the identical circumstances. In reason, comparing the effectiveness of the 2, 3 and 4-layer shells, on average, specimens provide results for the flexural strength (f) that are quite near to each other, with values ranging from 753.4 MPa to 815.4 MPa. The part printed at 4-layer shell, however, performed better than its contemporaries. The average flexural results for each layer height (0.15, 0.2, and 0.25 mm) show similarly decreased results, with values ranging from 815.4 MPa to 774.6 MPa (Fig. 5b). However, the 0.15 LH specimens outperformed their peers. The through-thickness vs in-plane resistance of the print layers may be the contributing factor to sample 7's superior performance. The top performing specimens from the current investigation, which were 0.15 mm LT, 4-layer shell, and 120 flow%, have been compared with data from other studies, as shown in Table 5.

Table 5: Comparison of tensile properties among 316L specimens fabricated by different means

Source	σf (MPa)	UTS (MPa)	Elongation at Break (%)
This work	141.9	426.6	36.4
Ait-Mansour et al. [25]	140.77	311.81	12.48
Gong et al. [36]	167	465	31
Liu et al. [16]	194	441	29.5
Rosnitschek et al. [37]	-	296	32
Damon et al. [38]	155	500	32

The total flexural strength values shown in Table 3, demonstrate that the results from the experiment are within the range of previously reported results, particularly for the component printed at 0.15 mm Lhand 120 flow%.

IV. CONCLUSION

A conclusion section is not required. Although a conclusion may review the main points of the paper, do not replicate the abstract as the conclusion. A conclusion might elaborate on the importance of the work or suggest applications and extensions.

In this work, the density, mechanical characteristics, and porosity that result from the sintering of an FFFm-printed SS316L part are examined, analysing the influence of three different printing parameters such as layer thickness, layer shell, and filament flow%. Therefore, the following conclusions were drawn.

1. After extensive analysis, it was found that by carefully adjusting the sintering parameters, it was possible to prevent the creation of hazardous phases (oxides) and achieve high sintering densities.

2. The sintered parts were comparted with conventional 316L parts and are demonstrated good mechanical properties. The experimental findings showed that the FFFm process parameters had an impact on the bulk density of the finished sintered components. The printing method with the greatest results in terms of maximum density specifically had a layer thickness of 0.15 mm, a layer count of 4, and 120 filament flow% (specimen 7).

3. Tensile results from tests were used to calculate the ultimate tensile strength and elongation at break. The specimen produced with 0.15 mm LT, a 4-layer shell, and a 120% filament flow (specimen 7) had the greatest UTS and elongation at break values of 464.1 MPa and 42% respectively. The specimen printed with 0.25 mm LT, a 2-layer shell, and 100% filament flow (specimen 6) had the lowest UTS and elongation at break values of 409.9 MPa and 37% respectively. These findings showed that a rise in LT causes a decrease in the part's strength.

4. The specimen produced with 0.15 mm LT, 4-LS, and 120% filament flow (specimen 7) showed the highest flexural strength (σf) 815.4 MPa, it was just 6.8% lesser than the AISI316L commercial material.

5. Large dimples near to one another and layer delamination for the greater layer thickness were found in the SEM analysis of fractured tensile and fracture impact test specimen data. Thus, the as-built multi-layered structure's outstanding ductility was clearly demonstrated by the findings.

6. Comparing metal extrusion to conventional metal AM methods, the former is a potentially more cost-effective method that eliminates handling powder and has a smaller carbon footprint. Despite its promising benefits, its use is limited to non-critical and high value added commercial based products like dyeing machines and pipes due to its alleviated mechanical characteristics and significant presence of porosity.

V. REFERENCES

[1] ASTM INternational, ISO/ASTM 52900:2015(E) Standard Terminology for Additive Manufacturing; ASTM: 2015.

[2] Jirsák, P.; Brunet-Thornton, R. Perspectives of Operational Additive Manufacturing Case Studies from the Czech Aerospace Industry. *J. East. Eur. Cent. Asian Res.* 2019, *6*, 179. DOI: 10.15549/ jeecar.v6i1.273.

[3] Delic, M.; Eyers, D. R.; Mikulic, J. Additive Manufacturing: Empirical Evidence for Supply Chain Integration and Performance from the Automotive Industry. *Supply Chain Manag*. 2019, *24*(5), 604. DOI: 10.1108/SCM-12-2017-0406.

[4] Fu, K.; Yao, Y.; Dai, J.; Hu, L.; Progress in 3D Printing of Carbon Materials for Energy-related Applications. *Adv. Mater.* 2017, *29*(9), 1603486. DOI: 10.1002/adma.201603486.

[5] Sames, W. J.; List, F. A.; Pannala, S.; Dehoff, R. R.; Babu, S. S. The Metallurgy and Processing Science of Metal Additive Manufacturing. Int. Mater. Rev. 2016, 61(5), 315. DOI: 10.1080/09506608.2015.1116649.

[6] Singh S, Ramakrishna S, Singh R. Material issues in additive manufacturing: a review. J Manuf Process 2017;25:185e200. https://doi.org/10.1016/j.jmapro.2016.11.006.

[7] G. Wu, N.A. Langrana, R. Sadanji, S. Danforth, Solid freeform fabrication of metal components using fused deposition of metals, Mater. Des. 23 (1) (2002) 97–105.

[8] P. Carreira, F. Cerejo, N. Alves, M.T. Vieira, In search of the optimal conditions to process shape memory alloys (NiTi) using fused filament fabrication (FFF), Materials 13 (21) (2020) 4718.

[9] C. Xu, B. Quinn, L.L. Lebel, D. Therriault, G. L'Espérance, Multi-material direct ink writing (DIW) for complex 3D metallic structures with removable supports, ACS Appl. Mater. Interfaces 11 (8) (2019) 8499–8506.

[10] J. Abel, U. Scheithauer, T. Janics, S. Hampel, S. Cano, A. Müller-K¨ohn, A. Günther, C. Kukla, T. Moritz, Fused Filament Fabrication (FFF) of metal-ceramic components, J. Vis. Exp. (143) (2019), e57693.

[11] A. Günther, T. Moritz, U. Mühle, Microstructure and interface characteristics of 17- 4PH/YSZ components after co-sintering and hydrothermal corrosion, Ceramics 3 (2) (2020) 245–257.

[12] Y. Zhang, L. Poli, E. Garratt, S. Foster, A. Roch, Utilizing fused filament fabrication for printing iron cores for electrical devices, 3D Print. Addit. Manuf. 7 (6) (2020) 279–287.

[13] Gill SS, Singh J, Singh R, Singh H. Effect of cryogenic treatment on AISI M2 high speed steel: metallurgical and mechanical characterization. J Mater Eng Perform 2012;21:1320e6. https://doi.org/10.1007/s11665-011-0032-z.

[14] K. Weman, Welding Processes Handbook, Elsevier, 2011, pp. 191–206.

[15] A. Bautista, F. Velasco, M. Campos, M. Rabanal, J. Torralba, Oxidation behavior at 900◦C of austenitic, ferritic, and duplex stainless steels manufactured by powder metallurgy, Oxidation Metals 59 (3) (2003) 373–393.

[16] B. Liu, Y. Wang, Z. Lin, T. Zhang, Creating metal parts by fused deposition modeling and sintering, Mater. Lett. 263 (2020) 127252.

[17] Y. Wang, L. Zhang, X. Li, Z. Yan, On hot isostatic pressing sintering of fused filament fabricated 316L stainless steel–evaluation of microstructure, porosity, and tensile properties, Mater. Lett. 296 (2021) 129854.

[18] A. Watson, J. Belding, B.D. Ellis, Characterization of 17-4 PH processed via bound metal deposition (BMD), in: TMS 2020 149th Annual Meeting & Exhibition Supplemental Proceedings, Springer, 2020, pp. 205–216.

[19] M.Á. Caminero, A.R. Gutiérrez, J.M. Chacón, E. García-Plaza, P.J. Núñez, Effects of fused filament fabrication parameters on the manufacturing of 316l stainless-steel components: Geometric and mechanical properties, Rapid Prototyp. J. (ahead-of-print) (2022).

[20] M. Quarto, M. Carminati, G. D'Urso, Density and shrinkage evaluation of AISI 316L parts printed via FDM process, Mater. Manuf. Process. 36 (13) (2021) 1535–1543.

[21] A. Boschetto, L. Bottini, F. Miani, F. Veniali, Roughness investigation of steel 316L parts fabricated by metal fused filament fabrication, J. Manuf. Process. 81 (2022) 261–280.

[22] C. Burkhardt, P. Freigassner, O. Weber, P. Imgrund, S. Hampel, Fused filament fabrication (FFF) of 316L green parts for the MIM process, World PM2016-AM-Depos. Technol. (2016).

[23] D. Jiang, F. Ning, Additive manufacturing of 316L stainless steel by a printingdebinding- sintering method: Effects of microstructure on fatigue property, J. Manuf. Sci. Eng. 143 (9) (2021).

[24] Thompson Y, Gonzalez-Gutierrez J, Kukla C, Felfer P. Fused filament fabrication, debinding and sintering as a low-cost additive manufacturing method of 316L stainless steel. Addit Manuf 2019;30:100861.

[25] Ait-Mansour I, Kretzschmar N, Chekurov S, Salmi M, Rech J. Design-dependent shrinkage compensation modeling and mechanical property targeting of metal FFF. Prog Addit Manuf 2020;5(1):51–7.

[26] Tosto C, Tirillo J, Sarasini F, Cicala G (2021) Hybrid metal/polymer filaments for fused filament fabrication (FFF) to print metal parts. Appl Sci 11:1444. https:// doi. org/ 10. 3390/ app11 041444

[27] Carminati M, Quarto M, D'urso G et al (2022) Mechanical characterization of AISI 316L samples printed using material extrusion. Appl Sci. https:// doi. org/ 10. 3390/ app12 031433

[28] Marius A. Wagner, Amir Hadian, Tutu Sebastian, Frank Clemens, Thomas Schweizer, Mikel Rodriguez-Arbaizar, Efrain Carreño-Morelli, Ralph Spolenak, "Fused filament fabrication of stainless steel structures - from binder development to sintered properties", Additive Manufacturing, Volume 49, 2022, 102472, ISSN 2214-8604, https://doi.org/10.1016/j.addma.2021.102472.

[29] Anirudh Kasha, Solomon O. Obadimu, Kyriakos I. Kourousis, Flexural characteristics of material extrusion steel 316L: Influence of manufacturing parameters, Additive Manufacturing Letters, Volume 3, 2022, 100087, ISSN 2772-3690, https://doi.org/10.1016/j.addlet.2022.100087.

[30] Pellegrini, A., Palmieri, M.E., & Guerra, M.G. Evaluation of anisotropic mechanical behaviour of 316L parts realized by metal fused filament fabrication using digital image correlation. *Int J Adv Manuf Technol* **120**, 7951–7965 (2022). https://doi.org/10.1007/s00170-022-09303-z

[31] Sun Y, Moroz A, Alrbaey K. Sliding wear characteristics and corrosion behavior of selective laser melted 316L stainless steel. J Mater Eng Perform 2014;23:518–26.

[32] Sander J, Hufenbach J, Giebeler L, Bleckmann M, Eckert J, Kuehn U. Microstructure, mechanical behavior, and wear properties of FeCrMoVc steel prepared by selective laser melting and casting. Wear 2017;126:41–4.

[33] Bartolomeu F, Buciumeanu M, Pinto E, Alves N, Carvalho O, Silva F, Miranda G. 316L stainless steel mechanical and tribological behavior—a comparison between selective laser melting, hot pressing and conventional casting. Addit Manuf 2017;16:81–9.

[34] Oliveira, R.V.B.; Soldi, V.; Fredel, M.C.; Pires, A.T.N. Ceramic injection moulding: Influence of specimen dimensions and temperature on solvent debinding kinetics. J. Mater. Process. Technol. 2005, 160, 213–220. [CrossRef]

[35] Kurose, T.; Abe, Y.; Santos, M.V.A.; Kanaya, Y.; Ishigami, A.; Tanaka, S.; Ito, H. Influence of the Layer Directions on the Properties of 316L Stainless Steel Parts Fabricated through Fused Deposition of Metals. Materials 2020, 13, 2493. [CrossRef].

[36] Gong, H.; Snelling, D.; Kardel, K.; Carrano, A. Comparison of Stainless Steel 316L Parts Made by FDM- and SLM-Based Additive Manufacturing Processes. JOM 2019, 71, 880–885.

[37] Rosnitschek, T.; Tremmel, S.; Seefeldt, A.; Alber-Laukant, B.; Neumeyer, T.; Altstädt, V. Correlations of geometry and infill degree of extrusion additively manufactured 316l stainless steel components. Materials 2021, 14, 5173.

[38] Damon, J.; Dietrich, S.; Gorantla, S.; Popp, U.; Okolo, B.; Schulze, V. Process porosity and mechanical performance of fused filament fabricated 316L stainless steel. Rapid Prototyp. J. 2019, 25, 1319–1327.

[39] ASTM A666-15; Standard Specification for Annealed or Cold-Worked Austenitic Stainless-Steel Sheet, Strip, Plate, and Flat Bar; ASTM International: West Conshohocken, PA, USA, 2014

AUTHORS

First Author – Dr. SAGAR M Baligidad, B.E., M.Tech., Ph.D., CMR Institute of Technology, sagar.mb@cmrit.ac.in

Second Author – Dr. Batluri Tilak Chandra, B.E., M.Tech., Ph.D., Sri Siddartha Institute of Technology and batluritilakchandra@ssit.edu.in

Third Author – Girish S.M, Research scholar, Sri Siddartha Institute of Technology and girishsmahadevaiah1@gmail.com